Title
Motion resilience of the balanced steady-state free precession geometric solution

Journal
Magnetic Resonance in Medicine, 89(1)

ISSN
0740-3194

Authors
Hoff, Michael N
Xiang, Qing-San
Cross, Nathan M
et al.

Publication Date
2023

DOI
10.1002/mrm.29438

Peer reviewed

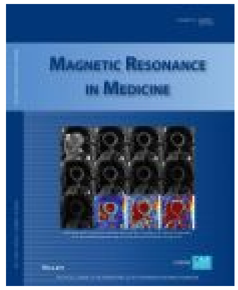

Motion Resilience of the Balanced Steady State Free Precession Geometric Solution

Journal:	*Magnetic Resonance in Medicine*
Manuscript ID	Draft
Wiley - Manuscript type:	Research Article
Research Type:	Artifacts < Technique Development
Research Focus:	No specific tissue or organ focus

Motion Resilience of the Balanced Steady State Free Precession Geometric Solution

Michael N. Hoff, PhD[1], Qing-San Xiang, PhD[2,3], Nathan M Cross, MD MS[4], Daniel Hippe, MS[5], Jalal B. Andre, MD[4]

[1]Department of Radiology and Biomedical Imaging, University of California San Francisco, San Francisco, CA, USA

[2]Department of Physics & Astronomy, University of British Columbia, Vancouver, BC, Canada

[3]Department of Radiology, University of British Columbia, Vancouver, BC, Canada

[4]Department of Radiology, University of Washington, Seattle, WA, USA,

[5]Clinical Biostatistics, Fred Hutchinson Cancer Research Center, Seattle, WA, USA

The 'Geometric Solution' was published by Xiang Q-S and Hoff MN: "Banding artifact removal for bSSFP imaging with an elliptical signal model" in Magn Reson Med 2014;71(3):927-933.

Some of the Geometric Solution motion studies in this manuscript were presented in abstract form at various ISMRM meetings, including "Correction in Temporal Bone Imaging with GS-bSSFP" in Milan, 2014, "On the Resilience of GS-bSSFP to Motion and other Noise-like Artifacts" in Toronto, 2015, "Evaluating Motion Artifact Correction of the Linearized Geometric Solution in bSSFP MRI." in Paris, 2018, and "The Geometric Solution to Banding Mitigates Motion Artifact in bSSFP Imaging." in the 2020 virtual meeting.

Running Title: Geometric Solution bSSFP Motion Resilience

Corresponding author:

Michael N. Hoff, Ph.D.
Department of Radiology and Biomedical Imaging, University of California, San Francisco
505 Parnassus Ave, San Francisco, CA 94143
E-mail: michael.hoff2@ucsf.edu
Tel: (206) 557-2736

Total word count = 4411

Total Tables + Figures = 10

Abstract

Purpose: Many MRI sequences are sensitive to motion and its associated artifacts. The Linearized Geometric Solution (LGS), a balanced Steady State Free Precession (bSSFP) off-resonance signal demodulation technique, is evaluated with respect to motion artifact resilience.

Theory and Methods: The mechanism and extent of LGS motion artifact resilience is examined in simulations, flow phantom experiments, and in vivo clinical evaluations. Motion artifact correction capabilities are decoupled from susceptibility artifact correction when feasible to permit controlled analysis of motion artifact correction when comparing the LGS with standard and phase-cycle-averaged bSSFP (complex sum, CS) imaging.

Results: Simulations revealed that aside from some scenarios with low image signal or slow motion, the LGS shows a stronger propensity than standard clinical bSSFP imaging techniques for motion artifact reduction. Flow phantom experiments asserted that the LGS reduces short-duration motion artifact error by ~6x relative to other bSSFP methods but for constant motion yields only ~40% error reduction. In vivo analysis demonstrated that in the IAC/orbits, the LGS was deemed to have less artifact than the CS in 24%/49% of reads (similar artifact in 76%/51% of reads), and less artifact than standard bSSFP in 97%/81% of reads (similar artifact in 3%/16% of reads). Only two of 63 reads deemed the LGS inferior to either CS or standard bSSFP in terms of artifact reduction.

Conclusion: The LGS provides bSSFP motion artifact reduction in addition to elimination of susceptibility artifacts, inspiring its use in a wide variety of applications.

Key words: bSSFP imaging; phase cycling; banding artifact; motion artifact; linearized geometric solution

Introduction

One of the most efficient clinical MRI pulse sequences is the balanced Steady State Free Precession (bSSFP) technique (1,2), which exhibits high SNR and efficiency owing to its spin-echo-like magnetization refocusing (3). This has led to widespread clinical utilization (4), where strong T1/T2 contrast ensures its applicability to scenarios requiring clear differentiation of tissue from fluid (5). Cardiac imaging and angiography benefit from bSSFP's sharp discrimination of muscle and blood. Globe imaging benefits from strong aqueous/vitreous humor signal that is well delineated from the lens. The inner ear's endolymph/perilymph-containing structures are well contrasted from finely structured surrounding tissue, making bSSFP MRI of the temporal bone ideal for diagnosing pathologies such as congenital ear anomalies, semicircular canal dehiscence, vestibular schwannoma, and inner/middle ear lesions (6). High bSSFP CSF signal permits clear visualization of cisternal cranial nerve segments (7), discrimination of lesions from the spinal cord and epidural structure margins within the intradural, extramedullary space, and myelographic evaluation of the subarachnoid space (8,9).

Unfortunately, MRI methods suffer from artifacts, and bSSFP is no exception. Images are often marred by uneven signal intensity and dark bands due to regional variations in the magnetic field that yield off-resonant phase accumulation between RF pulses (10). Patient motion is also a concern, despite bSSFP's speed and balanced gradients that reduce corresponding artifacts (11). Motion artifacts manifest in images as noise-like ghosts and darkened regions stemming from signal dephasing. They can occur in concert with off-resonant signal modulation, although it can be difficult to differentiate the two artifacts' individual contributions to general image quality degradation.

The linearized geometric solution (LGS) was originally developed to overcome off-resonance-induced signal modulation (12). Most methods of reducing the associated dark image bands use RF phase cycling (11,13) to increment the phase of sequential RF pulses and spatially shift the modulation. Bands are then suppressed by arbitrarily combining or averaging variably phase-cycled images (13-18), yielding band suppression that typically depends upon tissue/system parameters with banding spatial frequency increased by the number of phase-cycled images combined. Conversely, the LGS employs an analytic solution to the elliptical signal model that eliminates bSSFP dark banding and signal modulation, regardless of system parameters (12,19).

While the LGS demodulates bSSFP images of off-resonant effects, its influence on patient motion artifacts is uncertain. Any flow or bulk motion of patient tissue that occurs during or between the LGS' four required phase-cycled images might contaminate the reconstruction by disrupting the elliptical signal model, yielding artifacts that obscure pathology. Surprisingly, preliminary in vivo temporal bone, foramen magnum, and cervical spine imaging revealed that when processing the same four phase-cycled images, the LGS can actually mitigate motion artifact present in standard bSSFP imaging more extensively than a complex average (complex sum, CS)(20,21).

It is thus hypothesized that the LGS has a greater capacity for motion artifact minimization than other bSSFP-MRI techniques; here the motion artifact correction capabilities and limitations of the LGS-bSSFP, CS, and standard bSSFP imaging are evaluated and compared. Simulations are generated that mimic motion with variable amplitude, frequency, orientation, tissue type, and image noise. A water flow phantom emulates physiological flow with variable velocity and duration. These digital and physical simulations include analyses of signal deviation and total relative error from exact and non-motion gold standards to assess motion's effects on image reconstruction. In addition, imaging centered on the internal auditory canals (IAC) and orbits was performed on 21 volunteers, with artifact assessment scored by three blinded radiologists, and clinical feasibility demonstrated via statistical analysis. The goal was to ascertain the mechanism and extent of motion artifact correction and thereby infer the clinical potential of the LGS.

Theory

bSSFP Elliptical Signal Model

The complex bSSFP magnetization may be expressed by the following formulation (5,12,22):

$$I(\theta,t) = M\frac{1-E_2e^{i\theta}}{1-b\cos\theta}e^{i\varphi}e^{-t/T_2} + n$$

$$M = \frac{M_0\sin\alpha(1-E_1)}{1-E_1\cos\alpha-E_2^2(E_1-\cos\alpha)},\ b = \frac{E_2(1-E_1)(1+\cos\alpha)}{1-E_1\cos\alpha-E_2^2(E_1-\cos\alpha)} \quad [1]$$

$$a = E_2 = e^{-\mathrm{TR}/T_2}, \qquad E_1 = e^{-\mathrm{TR}/T_1}, \qquad \varphi = \gamma\Delta\mathrm{B}_0\cdot t \qquad \theta = \gamma\Delta\mathrm{B}_0\cdot\mathrm{TR}+\Delta\theta$$

$I(\theta,t)$ is the bSSFP magnetization at time t following the RF pulse, with off-resonant phase θ (modulo 2π) induced by the static magnetic field inhomogeneity $\Delta\mathrm{B}_0$. M_0 is the thermal equilibrium magnetization, T_1 and T_2 are the tissue relaxation times, n is the bivariate noise, $\Delta\theta$ is the phase-cycling increment, and α is the RF flip angle. For continuous $\theta = 0\rightarrow2\pi$, $I(\theta,0)$ traces out an ellipse in the complex signal plane as shown in Fig. 1 (12). Note that the factor e^{-t/T_2} typically approaches unity and uniformly diminishes all signal values. Additionally, if $t \neq 0$, the phase factor $e^{i\varphi}$ essentially rotates the ellipse by an amount $\varphi = \gamma\Delta B_0 \cdot t$ (modulo 2π), so in the reference frame of the ellipse the bSSFP signal may be expressed more simply as $I(\theta)$.

Geometric Solution and Linearization

Figure 1 shows that a line in the complex plane connecting any two data points $I(\theta_1)$ and $I(\theta_1 + \pi)$ on the signal ellipse will always pass through a point M. Six such "spokes" are depicted, although only two ellipse spokes are required for localization of this intersectional cross-point. Consider two spokes connecting $I_1 = I(\theta_1)$ to $I_3 = I(\theta_1 + \pi)$ and $I_2 = I(\theta_2)$ to $I_4 = I(\theta_2 + \pi)$; analytically, a geometric solution (GS) may be formed to localize M:

$$M = \frac{(x_1y_3 - x_3y_1)(I_2 - I_4) - (x_2y_4 - x_4y_2)(I_1 - I_3)}{(x_1 - x_3)(y_2 - y_4) - (x_2 - x_4)(y_1 - y_3)} \qquad [2]$$

where x_i and y_i represent the real and imaginary components respectively of a pixel from the i^{th} image I_i. The Linearized Geometric Solution (LGS) is formed to improve SNR as detailed in Xiang and Hoff (12), where following regularization of the GS, linearization is achieved by minimizing distance from a elliptical spoke in forming a regional weighted average of the corresponding pair of ellipse points.

Noise Radiality

Motion's complex signal plane manifestation is noise-like. This is displayed in Fig. 1, labeled "$I(\theta_1) + n$" (signal + noise). Rotation of the frame of reference such that the noise is described in terms of its radial (N_r) and tangential (N_t) components with respect to a spoke passing through M permits definition of the data sample's noise "radiality"

$$\varrho = \frac{N_r - N_t}{N_r + N_t} \qquad [3]$$

such that $\varrho = {+1}/{-1}$ corresponds to purely radial/tangential noise. The ϱ-value for a pixel is given by the summed radial N_r and tangential N_t noise components for all input ellipse signal values.

Error Metrics

Reconstructed image pixel magnitudes are given by I_i (say I_{LGS} or I_{CS}), and x, y represent pixel locations. Regional comparisons of different solutions are possible by computing the Total Relative Error (23) TRE, the normalized square-root pixelwise sum of square differences of I_i from its gold standard I_g.

$$\text{TRE} = \frac{\sqrt{\sum_{x,y}[I_i(x,y) - I_\mathrm{g}(x,y)]^2}}{\sum_{x,y} I_\mathrm{g}(x,y)} \quad [4]$$

Quantification of relative flow artifact in the flow phantom experiments is computed via the error energy EE. This is formed from the pixelwise sum of the square differences between flow-compromised and relatively static solutions:

$$EE = \sum_{x,y} [I_i(x,y)_{flow} - I_i(x,y)_{no-flow}]^2 \quad [5]$$

Methods

MATLAB (The Mathworks, Inc., Natick, MA, USA) code for the described algorithms have been posted online at https://github.com/mnhoff/GS-bSSFP_MotionStudy.

All digitally simulated, experimental phantom, and in vivo data discussed below involved simulation/acquisition of i = 1, 2, 3, and 4 respectively phase cycled $\Delta\theta$ = 0°, 90°, 180°, and 270° datasets to emulate varied bSSFP ellipse signal points. The GS was computed by Eq. [2], and the LGS was then formed by regulating and linearizing the GS as described (12). The CS was computed from the normalized complex signal average, and magnitude images were computed for all image reconstructions. For multiple-RF-channel datasets, reconstructions were formed for each coil followed by pixel-by-pixel combination via sum-of-squares across all coils.

Simulation Methods

Two simulations employed Eq. [1] to simulate the four phase-cycled bSSFP datasets with TR = 4.2 ms, spatially varying T_1 = 200 → 3000 ms, T_2 = 40 → 3000 ms through the parameters a and b, off-resonant accumulated phase θ ranging from $-\pi$ to π, and added zero-mean bivariate Gaussian noise.

Simulation 1: All four phase-cycled images were simulated using α = 70° and multiplied by a binary magnitude mask of basic shapes to introduce structure as shown in Fig. 2 (24). The $\Delta\theta$ = 0° dataset's signal region was incrementally translated in one dimension to oscillate at a specific frequency and amplitude, yielding a series of motion frames. A 2D Fourier Transform (2DFT) was applied to each frame to yield a time-series of k-space frames. This 3D k-t block was obliquely sampled by collecting spatially-sequential lines (parallel to motion for phase encoding (PE) direction motion artifacts, perpendicular to motion for frequency encoding (FE) direction motion artifacts) from temporally-sequential k-space frames to form a single 2D motion-corrupted k-space (25). An inverse 2DFT was applied to give the motion-corrupted image; an example image with PE-directed 3-pixel motion amplitude and 40 cycles/dataset motion frequency is shown in Fig. 2a. Figure 2a-d shows all four phase-cycled images (the first corrupted by motion) subsequently used to compute the e. LGS and f. CS as described above (24).

The Fig 2a. simulation was repeated at variable motion amplitude (0-30 pixels shifts) and frequency (0-60 cycles per dataset), with TRE computed for the LGS (I_{LGS}) and the CS (I_{CS}) relative to solutions of data without motion corruption (I_g). Figure 3 depicts 3D surface plots of these TRE values vs variable motion frequency and amplitude for both a. PE and b. FE motion.

Figure 2a-d data was also simulated at different noise values with the LGS and CS computed for each, and corresponding TRE values were plotted vs. noise in Fig 4a. The same data was also simulated with spatially constant T1 and T2 but varied T1/T2 ratio in multiple phase-cycled datasets, and the corresponding LGS and CS TRE values were plotted vs T1/T2 ratio in Fig 4b (24).

Simulation 2: Figures 5 a-d illustrate a second simulation using $\alpha = 80°$ and a parameter variation extended through 10 cycles of $\theta = -\pi$ to π to generate more data for statistical power. The noise radiality ϱ was computed pixelwise from corresponding phase-cycled data (phase cycles), and solution signal errors were found from the difference between the CS, GS, and LGS reconstructed signal and their respective gold standards. Gold standards are M for the GS and LGS, and the center of mass of the elliptical data points for the CS (12). Signal errors were scatterplotted pixel-by-pixel as a function of the noise radiality ϱ of the reconstructed pixel's source data in Fig 6a-c. Pixels were then partitioned into 50 bins according to their radiality ϱ values, and for each bin the standard deviation and bias of the corresponding CS, GS and LGS values were computed and plotted in Fig. 6d (26). Bias error bars were computed using 95% confidence intervals of the signal error data.

Experimental Flow Phantom Methods

Plastic tubing with a 0.64 cm inner diameter was coiled around a 4L plastic bottle of water and placed in the MRI scanner. Water was pumped through the tube at controlled velocity and duration using an Arduino-circuit-controlled linear actuator and plastic syringes located outside the scanner room; see Supporting Information Fig. S1 for photographs. Four phase cycles were acquired on a 3T Philips Healthcare (Best, Netherlands) Achieva dStream scanner using $\alpha = 30°$, TR/TE = 4.60/2.30 ms, 214 s total scan time, 128/108/90 matrix size and 2.0/2.0/2.0 mm voxel size along frequency/phase/slice directions. Figure 7 depicts images acquired "0." without flow, and with "1." 40ml/60s, "2." 40ml/40s, and "3." 40ml/20s flow velocity during one phase cycle (1PC = 0°), and "4." 40ml/60s, "5." 40ml/40s, and "6." 40ml/20s flow velocity during all phase cycles (4PC). Delays of several minutes were inserted following 1PC flow to ensure a lack of flow during the remaining three phase cycles.

Once the LGS and CS were computed, flow artifact was visualized for each flow scenario X by computing the difference of the flow reconstruction from its "0": non-flow reconstruction, i.e. $\Delta LGS = |LGS_X - LGS_0|$ and $\Delta CS = |CS_X - CS_0|$, with signal normalized by the maximum over all difference maps to facilitate comparison at Fig. 7 right. The error energy EE of each difference map, normalized by the minimum EE value, was then computed to estimate total flow artifact EE as a function of flow speed as shown at the top-right of Fig. 7 (27).

In Vivo Methods

All in vivo studies included four phase cycles acquired in 3D mode on a 3T Philips Healthcare (Best, Netherlands) Ingenia scanner, followed by application of the LGS and CS reconstructions.

Preliminary proof-of-concept data shown in Fig. 8 employed a transmit/receive head coil to acquire axial temporal bone images with α = 30°, TE/TR = 4.2/2.1ms, and 180/180/120 matrix size and 1/1/1 mm voxel size along frequency/phase/slice directions (20).

An institutional review board approved 21 patients undergoing a clinically indicated temporal bone (IAC protocol) MRI for evaluation of treated vestibular schwannoma to receive added bSSFP sequences in both sagittal (average scan time = 3.9 min) and axial (average scan time = 5.8 min) orientations. Scan parameters were α/TR/TE = 30°-45°/4.8-5.5ms/1.9-2.2ms, and 316/314-316/42-100 matrix size and 0.57/0.57/1mm voxel size along frequency/phase/slice directions. The LGS and CS were computed and signal-normalized to avoid bias (27).

Three fellowship-trained neuroradiologists blinded to sequence type, imaging parameters, clinical presentation, and patient disposition evaluated standard bSSFP ($\Delta\theta$ = 180°), LGS-bSSFP, and CS-bSSFP images for the degree of dark artifact in the IAC and orbits of each patient using a 5-point Likert scale (1 = significant artifact to 5 = no artifact). Sample images may be seen in Fig. 9. The degree of dark artifact was compared between techniques using the Wilcoxon signed-rank test and clustered by subject to account for multiple readers as shown in Fig. 10 (27). The Wilcoxon signed-rank test does not make any assumptions about the distribution of the ratings and is appropriate for ordinal data. The test assumes that the subjects are independent but does not assume that the three reads of each subject are independent.

Results

Simulation Results

Simulation 1: Figure 2 exhibits the e. LGS with greater signal demodulation than the f. CS, which suffers from residual banding. The LGS also robustly eliminates noise-region ghosting artifacts that prevail in the CS, although some residual motion artifact is evident in both reconstruction's signal regions.

Figure 3 indicates that the LGS (green) has lower error than the CS (red) in most motion amplitude and frequency instances tested, aside from some slower low-frequency, mid-to-high-amplitude PE motion. Sample $\Delta\theta = 0°$ motion-corrupted images are inset at select motion parameter values for context. Figure 4 reveals that the LGS provides better motion correction than the basic averaging of the CS for images with greater SNR, as occurs with lower T1/T2 value or image noise. However, the CS performs similarly or better for bSSFP regions with lower SNR due to higher T1/T2 or noise.

Simulation 2: Figure 6 a-c illustrates that the GS has reduced error when noise is more radially oriented, and that the LGS generally has less error than the CS. Figure 6d confirms that the LGS balances the advantages and disadvantages of the GS to achieve less error deviation than the CS with almost zero bias for all radiality values. The CS has a consistent small non-zero bias at all radiality values, while the GS has a small non-zero bias for tangential noise regions but no bias for radial noise regions. Bias error bars were larger at extreme radiality values primarily due to the lower sample sizes in their respective bins.

Experimental Flow Phantom Results

Figure 7 depicts the physical flow phantom reconstructions with a.ΔLGS and b.ΔCS "flow – no-flow" image differences at far right and normalized flow artifact error energy EE given in green and red respectively for each flow scenario. Observation of these images and the upper-right plot of EE vs. flow rate depicts that the LGS EE is about 1/6th of the corresponding CS EE for the 1PC flow scenarios, but only reduces error by 40% when motion endures for the entire four-image scan. While increased flow velocity and duration do not have significant effect on the CS EE, increased flow duration yields increased EE for the LGS reconstruction, which consistently corrects artifact in the main bottle if not always in the tubes.

In Vivo Results

The proof-of-concept brain phase cycles in Fig. 8 demonstrate banding, spurious regional signal heterogeneity, and periodic motion artifact along the PE direction stemming from globe motion, CSF pulsation, and carotid arterial flow – especially in the $\Delta\theta = 90°$ foramen magnum image. Colored arrows in the CS show that this reconstruction suffers from residual banding in the globes (green) and CSF (yellow), erroneous contrast in the nasopharynx and prevertebral space (blue), and residual vascular and

CSF flow artifact (red). Equivalently colored arrows in the LGS indicate that nearly all artifacts are eliminated relative to the CS.

Sample orbit images from the multi-patient reader study shown on the left of Fig. 9 indicate that the LGS exhibits sharp margins of the bulbus oculi and relatively minimal vitreous darkening compared with the CS and standard bSSFP. Images of the IAC from a different patient shown on the right of Fig. 9 demonstrate good LGS contrast and cranial nerve demarcation, with slightly better CSF homogeneity when compared to the other imaging techniques.

Figure 10 reveals the statistical analysis of the three radiologists' assessments of dark artifacts in the three reconstructions over the 21 patients (3 radiologists x 21 patients = 63 reads). The scored LGS images were deemed to have on average slightly less dark artifact in the IAC than the CS images and much less than standard bSSFP images, with p-values = 0.001 and <0.001 respectively. The LGS had less artifact than the CS in 24% (15/63) and similar artifact in 76% of IAC reads (48/63), and had less artifact than bSSFP in 97% (61/63) and similar artifact in 3% of IAC reads (2/63); LGS images were never rated to have more dark artifact in the IAC than the CS or standard bSSFP images. In the orbits, the evaluated LGS images were found to have significantly less dark artifact in the globes than both the CS and standard bSSFP (p<0.001 for both). The LGS had less artifact than the CS in 49% (31/63) and similar artifact in 51% of orbits reads (32/63), and had less artifact than bSSFP in 81% (51/63), similar artifact in 16% (10/63), and more artifact in 3% of orbits reads (2/63); LGS images were never rated to have more dark artifact in the orbits than the CS images.

Discussion

This study confirms that beyond correction of magnetic field inhomogeneity artifacts, LGS-bSSFP has the propensity to mitigate motion artifacts. Evaluation of simulations, phantom imaging, and in vivo imaging indicates that the LGS generally exhibits less motion artifact than both complex averaging of phase-cycled bSSFP images and standard bSSFP imaging. Here the extent of motion artifact correction is elucidated, with emphasis on how motion duration, frequency, amplitude, and orientation affect solution accuracy. Overall, LGS-bSSFP represents an attractive imaging methodology due to its efficiency, tissue/fluid contrast, and artifact resilience.

This manuscript's primary concern is whether the LGS reconstruction will be disrupted by patient motion during one or more phase cycles. The elimination of motion artifact in the Fig. 8 proof-of-concept in vivo LGS images considering the motion corruption evident in the Fig. 8h $\Delta\theta = 90°$ phase cycle inspired the hypothesis that the LGS has some insensitivity to motion. The first "shapes" simulation confirmed this for

1PC motion, where Fig. 2 shows that motion artifacts were eliminated in the LGS' noise regions and suppressed in its signal regions. Flow phantom experiments further validated that the LGS advantageously mitigates flow artifact relative to the CS for 1PC flow, although motion during all phase cycles rendered the LGS performance to a comparable level with the CS, especially in regions of tube flow. The second "radiality" simulation provides some insight into why motion artifact is mitigated in the LGS. Motion manifests in a noise-like fashion, and the GS is insensitive to corresponding signal deviations oriented in a radial direction in the complex plane with respect to one of the two spokes used to localize the GS cross-solution (26).

Noise radiality is thus a key factor in determining the LGS' ability to correct motion artifacts, although it is not the only consideration. The radiality metric is important in the general situation when the four phase cycled signal values are at non-zero points on the bSSFP ellipse in the complex plane. However, in noise regions most signal values will be near the complex-plane origin. If one phase cycle noise region has non-zero signal due to a motion-induced ghost, the GS cross-point will still be localized near the origin and thus the artifact eliminated. Since the LGS uses the GS as a guide, artifacts in the GS (or lack thereof) are propagated into the LGS. Fortunately, the cumulative error simulation #2 showed that the LGS balances the GS' sensitivity to tangential noise with its resilience to radial noise to achieve error reduction that consistently undercuts the CS regardless of noise radiality.

The choice of gold standard for error calculations plays a key role in solution performance evaluation. Simulation #2 (Fig. 5 and 6) sought to investigate noise radiality's effects on solution performance, requiring an exact ground truth for its gold standard in the computation of the pixel-by-pixel overall displacement error. For the LGS and GS, this is simply the cross-point M, an exact solution that may be localized with four data points on the noiseless ellipse. But the ellipse is asymmetrically populated, so generally four points will only approximate the CS ground truth center-of-mass (12), leading to inherent bias in CS error calculations (as seen in Fig. 6d). The other simulation and phantom experiments were focused on only measuring motion-induced error, and thus use non-motion solution reconstructions as gold standards. The lack of artifactual signal in the Fig. 7 LGS_0 non-motion gold standard image hints that it is near the ground truth M cross-point. On the other hand, the non-motion gold standard CS_0 image in Fig. 7 displays residual off-resonance-induced banding artifact in the water bottle. These artifacts along with those from tube-flow are propagated into the flow artifact ΔCS difference maps. This infers a transient character to CS' residual banding, likely due to susceptibility artifact variation over time due to subtle bulk water motion.

Experimental conditions should thus also be considered when drawing conclusions from this study. Imaging gradient coil vibrations and/or nearby water tube flow may have disrupted the originally static water in the large bottle, and the error energy performance metric enumerates both these motion-susceptibility artifacts from subtle aqueous motion and the deliberate flow artifact. Additionally, consistent and accurate tube flow may have been deterred by turbulence, with fluid dynamics estimations of water in the narrow tubes suggesting that flow could be turbulent at all rates chosen. Other flow speed ranges or tube diameters may have thus yielded more predictable results. Reader bias, fatigue, and misunderstanding may have also occurred in the radiologist group, biasing results.

The clinical approach taken in the in vivo reader survey includes comparing a standard clinical $\Delta\theta$ = 180° bSSFP image with the multi-image LGS and CS reconstructions. Since the Δθ = 180° phase cycle's image signal is centered in the bSSFP off-resonance magnitude profile pass band, intensity-modulated image signal has a minimal chance of displaying dark bands in regions of homogeneous magnetic field. Additionally, the single-phase cycle allows less time for motion artifacts to manifest. This could account for rare occurrences, such as in 2 of the 63 total radiologist reads, where the standard bSSFP sequence is perceived to have less artifact than the LGS. Digital and physical phantom studies did not compare the $\Delta\theta$ = 180° image with the LGS and CS multi-image reconstructions. The lack of a meaningful gold standard for base bSSFP imaging and the disparity of comparing single images with multi-image averages preclude this base sequence from providing useful, quantitative comparisons.

As mentioned previously, the LGS is robust over different tissue types, but is most efficacious in fluid regions with high SNR and lower T1/T2 (19). The LGS may be eclipsed by the CS of phase-cycled data when SNR is low, where the SNR gains of balanced averaging outweigh the benefits of coherent artifact correction. This realization is reinforced by the surface plot simulations. Here motion artifacts in the LGS can exceed those in CS images at low SNR levels experienced by high T1/T2 (> 6) ratio tissues such as liver, muscle, and brain matter. However, bSSFP imaging is typically employed clinically for visualization of tissue with low T1/T2, where the LGS' correction of both susceptibility and motion artifacts outshines CS' correction.

The LGS' reconstruction of four bSSFP images is a relatively simple and time efficient procedure. The Philips system employed easily facilitated the acquisition of $\Delta\theta$ = 0°, 90°, 180°, and 270° phase-cycled bSSFP images, and phase-cycling has also been executed on Siemens and General Electric systems with relative ease (12,16). Post-processing of these images is minimal since the LGS is analytical in nature. Additionally, due in part to the high efficiency of bSSFP imaging, acquisition of all four phase cycles for experimental data required at most a few minutes scan time, which can be further reduced in future iterations that employ imaging acceleration techniques such as simultaneous multislice (28) and compressed sensing

(29). As a first step to speeding up this acquisition, phase cycles were spread across breath-holds to permit robust artifact correction in temporally-demanding dynamic CINE imaging without requiring added imaging sequences (30).

The added discovery of the LGS' potential for motion artifact mitigation absolves concerns that the technique would be overwhelmed by the presence of motion. The duration of the motion is a key factor in assessing the degree of motion resilience, where the LGS is especially robust for 1PC motion although at worst performs similarly to the CS for continuous 4PC motion. The practicality and ease of its application should ultimately pave the way for clinical adoption, where scan-time savings techniques could further limit the effects of motion and ensure its suitability for time-sensitive applications such as CINE imaging.

Conclusion

The LGS reconstruction of bSSFP images introduces an attractive method to increase bSSFP's clinical viability by mitigating motion artifacts in addition to correcting magnetic field inhomogeneity-induced signal modulation and banding. Digital and physical simulations demonstrated that the technique shows general resilience to artifacts stemming from both motion and flow. Its high SNR efficiency and artifact correction capabilities indicate its potential clinical efficacy in scenarios that require strong tissue/fluid contrast and high SNR but suffer from field inhomogeneity and patient motion.

Acknowledgments

The authors would like to thank Dr. Charles Colip for clinical image assessment. Dr. Michael Hoff received funding assistance from the University of Washington Royalty Research Fund. Mr. Hippe received research funding from G.E. Healthcare, Philips Healthcare, Canon Medical Systems, USA, and from the Biostatistics Shared Resource of the Fred Hutch/University of Washington Cancer Consortium (P30 CA015704).

References

1. Carr H. Steady-state free precession in nuclear magnetic resonance. Phys Rev 1958;112:1693-1701.

2. Oppelt A, Graumann R, Barfuss H, Fischer H, Hartl W, Schajor W. FISP: a new fast MRI sequence. Electromedica 1986;54:15-18.

3. Scheffler K, Hennig J. Is TrueFISP a gradient-echo or a spin-echo sequence? Magn Reson Med 2003;49:395-397.

4. Scheffler K, Lehnhardt S. Principles and applications of balanced SSFP techniques. Eur Radiol 2003;13:2409-2418.

5. Freeman R, Hill H. Phase and intensity anomalies in fourier transform NMR. J Magn Reson 1971;4:366-383.

6. Mohan S, Hoeffner E, Bigelow DC, Loevner LA. Applications of Magnetic Resonance Imaging in Adult Temporal Bone Disorders. Magn Reson Imaging Clin N Am 2012;20(3):545-572.

7. Chavhan GB, Babyn PS, Jankharia BG, Cheng HL, Shroff MM. Steady-state MR imaging sequences: physics, classification, and clinical applications. Radiographics 2008;28(4):1147-1160.

8. Danagoulian GS, Qin L, Nayak KS, Colen RR, Mukundan S, Harris MB, Jolesz FA, Shankaranarayanan A, Copen WA, Schmidt EJ. Comparison of wideband steady-state free precession and T2-weighted fast spin echo in spine disorder assessment at 1.5 and 3 T. Magn Reson Med 2012;68(5):1527-1535.

9. Tanitame K, Tanitame N, Tani C, Ishikawa M, Takasu M, Date S, Otani K, Awai K. Evaluation of lumber nerve root compression using thin-slice thickness coronal magnetic resonance imaging: three-dimensional fat-suppressed multi-shot balanced non-steady-state free precession versus three-dimensional T1-weighted spoiled gradient-recalled echo. Jpn J Radiol 2011;29(9):623-629.

10. Zur Y, Stokar S, Bendel P. An analysis of fast imaging sequences with steady-state transverse magnetization refocusing. Magn Reson Med 1988;6:175-193.

11. Zur Y, Wood ML, Neuringer LJ. Motion-insensitive, steady-state free precession imaging. Magn Reson Med 1990;16:444-459.

12. Xiang Q-S, Hoff MN. Banding artifact removal for bSSFP imaging with an elliptical signal model. Magn Reson Med 2014;71(3):927-933.

13. Ernst RR; Varian Associates, assignee. Fourier Transform NMR Spectroscopy Employing a Phase Modulated RF Carrier. US patent 3,968,424. July 6, 1976.

14. Deimling M, Laub G. Constructive Interference in Steady State (CISS) for Motion Sensitivity Reduction. In Book of Abstracts: Society of Magnetic Resonance in Medicine, Amsterdam, The Netherlands, 1989. p. 842.

15. Casselman JW, Kuhweide R, Deimling M, Ampe W, Dehaene I, Meeus L. Constructive interference in steady state-3DFT MR imaging of the inner ear and cerebellopontine angle. AJNR Am J Neuroradiol 1993;14(1):47-57.

16. Bangerter NK, Hargreaves BA, Vasanawala SS, Pauly JM, Gold GE, Nishimura DG. Analysis of multiple-acquisition SSFP. Magn Reson Med 2004;51:1038-1047.

17. Cukur T, Bangerter NK, Nishimura DG. Enhanced spectral shaping in steady-state free precession imaging. Magn Reson Med 2007;58:1216-1223.

18. Elliott AM, Bernstein Ma, Ward Ha, Lane J, Witte RJ. Nonlinear averaging reconstruction method for phase-cycle SSFP. Magn Reson Imaging 2007;25:359-364.

19. Hoff MN, Andre JB, Xiang Q-S. Combined geometric and algebraic solutions for removal of bSSFP banding artifacts with performance comparisons. Magn Reson Med 2017;77(2):644-654.

20. Hoff MN, Wilson GJ, Xiang Q-S, Andre J. Artifact Correction in Temporal Bone Imaging with GS-bSSFP. In Proceedings of the 22nd Annual Meeting of the ISMRM, Milan, Italy, 2014. p. 1627.

21. Hoff MN, Xiang Q-S, Andre J. Spinal Cord Imaging with Demodulated bSSFP. In Proceedings of the 22nd Annual Meeting of the ISMRM, Milan, Italy, 2014. p. 1717.

22. Lauzon ML, Frayne R. Analytical characterization of RF phase-cycled balanced steady-state free precession. Concepts Magn Reson Part A 2009;34A:133-143.

23. Chang Z, Xiang Q-S. Highly accelerated MRI by skipped phase encoding and edge deghosting with array coil enhancement (SPEED-ACE). Med Phys 2006;33:3758.

24. Hoff MN, Xiang Q-S. Evaluating Motion Artifact Correction of the Linearized Geometric Solution in bSSFP MRI. In Proceedings of the 26th Annual Meeting of ISMRM, Paris, France, 2018. p. 4086.

25. Xiang Q-S, Henkelman RM. K-space description for MR imaging of dynamic objects. Magn Reson Med 1993;29(3):422-428.

26. Hoff MN, Andre JB, Xiang Q-S. On the Resilience of GS-bSSFP to Motion and other Noise-like Artifacts. In Proceedings of the 23rd Annual Meeting of ISMRM, Toronto, Canada, 2015. p. 818.

27. Hoff MN, Cross NM, Xiang Q-S, Hippe DS, Colip CG, Andre JB. The geometric solution to banding mitigates motion artifact in bSSFP imaging. In Proceedings of the 28th Annual Meeting of ISMRM, Virtual, 2020. p. 7455.

28. Muller S. Multifrequency selective rf pulses for multislice MR imaging. Magn Reson Med 1988;6(3):364-371.

29. Lustig M, Donoho D, Pauly JM. Sparse MRI: The application of compressed sensing for rapid MR imaging. Magn Reson Med 2007;58:1182-1195.

30. Fischer A, Hoff MN, Ghedin P, Brau ACS. Banding-artifact free bSSFP cine imaging using a Geometric Solution approach. In Proceedings of the 24th Annual Meeting of ISMRM, Singapore, 2016. p. 1827.

Figure Captions

Fig.1: bSSFP signal ellipse, with noise radial/tangential components and radiality ϱ depicted with respect to an elliptical spoke.

Fig.2: Simulation 1, bSSFP data with spatially varying T1, T2, and θ. Δθ = a. 0° (corrupted by vertical Phase Encoding-direction motion: 3 pixel-shift cycled 40x), b. 90°, c. 180°, and d. 270° phase-cycled magnitude images. e. Linearized Geometric Solution and f. Complex Sum of a.-d.

Fig.3: Motion correction total relative error (TRE) for the Linearized Geometric Solution and Complex Sum of four phase cycled bSSFP datasets (as in Fig. 2), with variable motion frequency and amplitude in the Δθ = 0° phase cycled image along the a. PE direction and b. FE direction. Sample Δθ = 0° motion-corrupted images are inset for specific motion frequency (10 and 50 cycles/dataset) and amplitude (3 and 28 pixels).

Fig.4: Motion correction Total Relative Error (TRE) for the Linearized Geometric Solution and Complex Sum of four phase cycled bSSFP datasets (as in Fig. 2) plotted for variable phase cycled image a. noise, and b. T1/T2 ratio.

Fig.5: Simulation 2, bSSFP data with spatially varying T1, T2, and θ. a. $\Delta\theta = 0°$, b. 90°, c. 180°, and d. 270° phase-cycled magnitude images. Corresponding solutions from these phase cycles are the: e. Center-of-Mass, gold standard for the f. Complex Sum, and g. Cross-point M, gold standard for the h. Geometric Solution and the i. Linearized Geometric Solution.

Fig.6: bSSFP a. complex sum (CS), b. geometric solution (GS), and c. linearized geometric solution (LGS) pixelwise reconstruction error cumulatively distributed as a function of noise radiality ϱ. d. CS, GS, and LGS standard deviation and bias of error from a-c plotted as a function of noise radiality ϱ. Bias includes 95% confidence interval error bars to indicate instability in regions of highly tangential or radial noise due to small sample size in corresponding bins.

Figure.7: Four bSSFP phase cycles (PC) $\Delta\theta = 0°$, 90°, 180°, and 270° are acquired of a water phantom with encircling tubes of water in 0:no-flow and six flow scenarios: 1PC ($\Delta\theta = 0°$)-duration flows at 1. 40ml/60s, 2. 40ml/40s, and 3. 40ml/20s and 4PC-duration flow at 4: 40ml/60s, 5: 40ml/40s, and 6: 40ml/20s velocities. The linearized geometric solution (LGS) and complex sum (CS) are computed for each of the 7 scenarios. Flow artifact images at right (ΔCS/ΔLGS) stem from flow - non-flow differences for all 6 flow scenarios, and for each the error energy (EE) is computed, normalized, and listed. EE values are plotted vs. flow velocity at top right.

Fig. 8: Demodulation of bSSFP brain images. bSSFP axial magnitude images of the inner ear (above) and foramen magnum (below) phase cycled by $\Delta\theta$ = a) & g) 0°, b) & h) 90°, c) & i) 180°, and d) & j) 270° respectively are shown. The Complex Sum (CS) of each set of phase cycles given in e) & k) has colored arrows indicating residual banding in the CSF (yellow) and globes (green), signal modulation in the prevertebral space (blue), and motion artifact (red). Arrows of equivalent colors in the Linearized Geometric Solution (LGS) images of f) & l) demonstrate near elimination of all artifacts.

Fig. 9: Standard phase-cycled $\Delta\theta$= 180° bSSFP axial acquisitions (a, b) are combined with three more bSSFP acquisitions ($\Delta\theta$= 0°, 90°, and 270°) to compute the complex sum (c, d) and LGS linearized geometric solution (e, f) for patient orbits (left) and the Internal Auditory Canal (IAC) (right). The LGS displays the least darkening artifact in the vitreous humor of the globes and cerebrospinal fluid in the IAC when compared with the others.

Fig. 10: Left, average degree of dark artifact is reflected for standard bSSFP, LGS, and CS reconstructions using a Likert 5-point scale from 1 = significant artifact to 5 = no artifact for a. IAC and c. orbits. Error bars indicate 1 standard deviation. Right, stacked columns show the % of reads that gauged LGS > CS or bSSFP (green), LGS = CS or bSSFP (grey), or LGS < CS or bSSFP (black) in terms of artifact minimization for b. IAC and d. orbits.

Sup. Fig. S1: a. Arduino circuit with automated controls, stepper motor, and linear actuator to oscillate syringe injection and introduce variable-speed water flow through tubes around a phantom. b. Phantom consists of flexible tubing wound around a bottle of water.

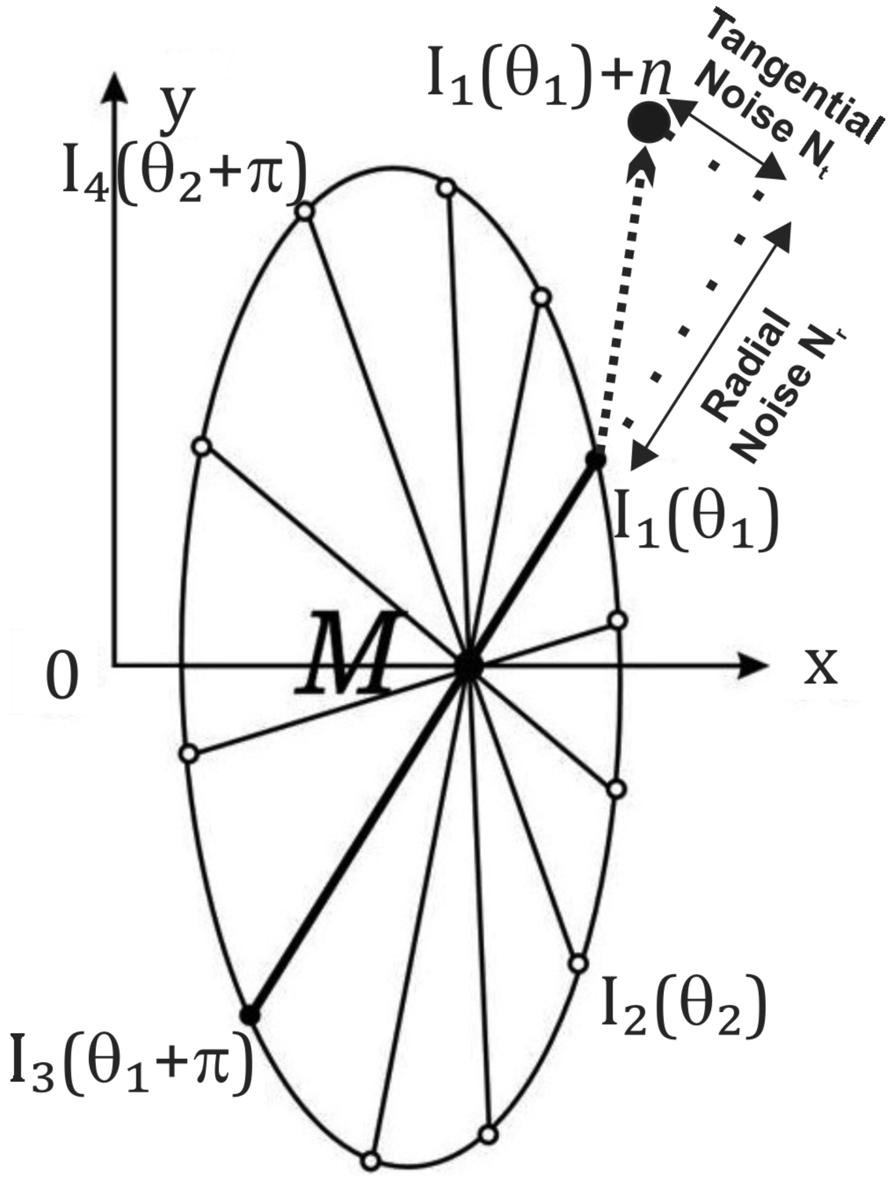

Fig.1: bSSFP signal ellipse, with noise radial/tangential components and radiality ϱ depicted with respect to an elliptical spoke.

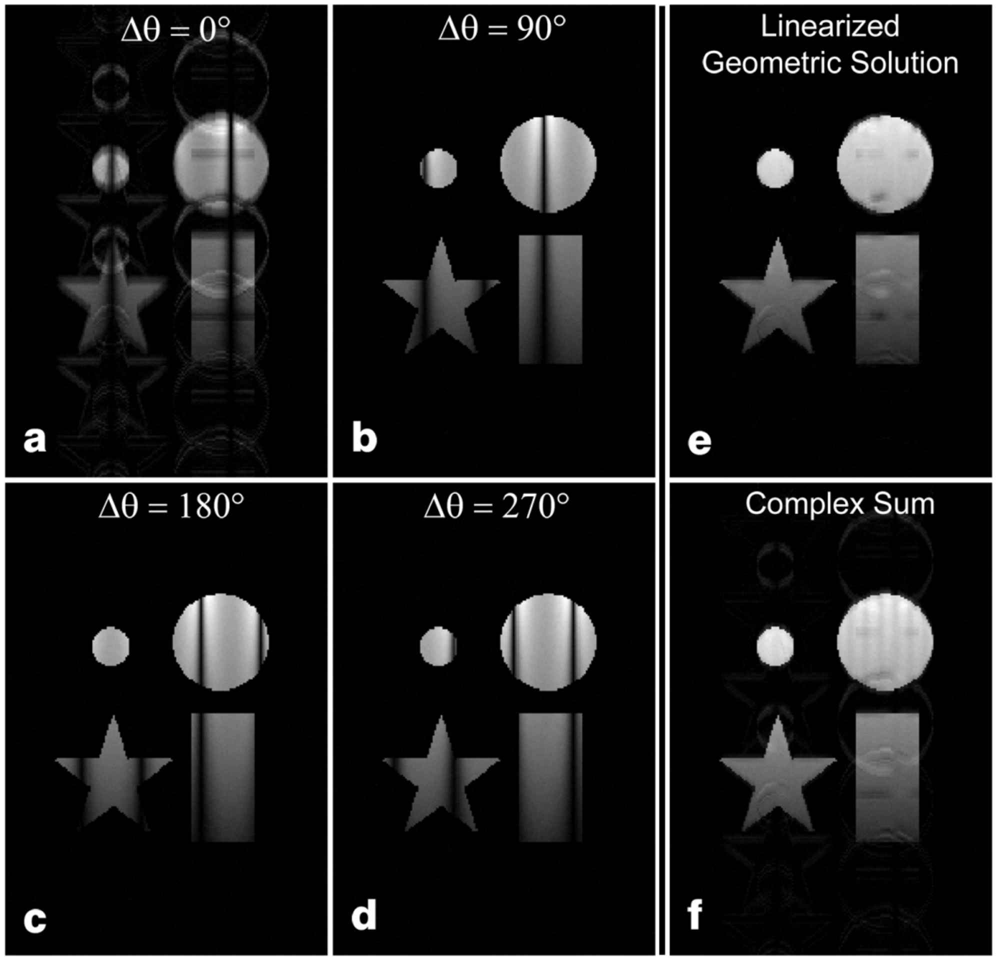

Fig.2: Simulation 1, bSSFP data with spatially varying T1, T2, and θ. Δθ = a. 0° (corrupted by vertical Phase Encoding-direction motion: 3 pixel-shift cycled 40x), b. 90°, c. 180°, and d. 270° phase-cycled magnitude images. e. Linearized Geometric Solution and f. Complex Sum of a.-d.

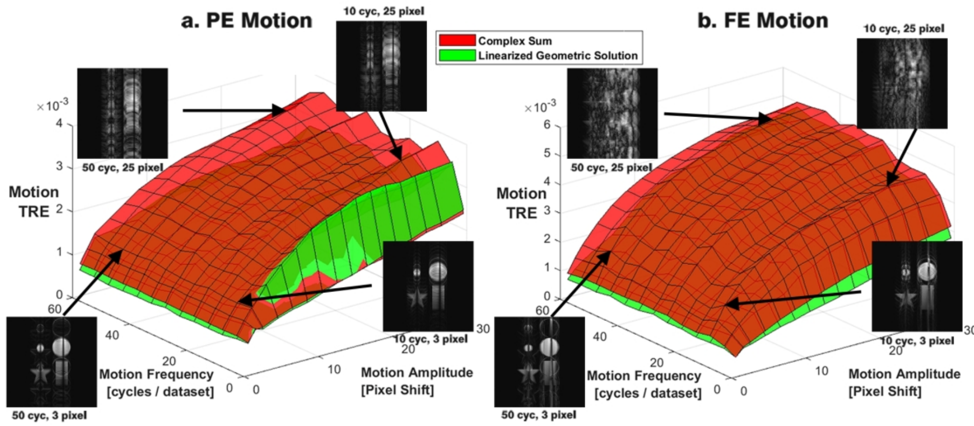

Fig.3: Motion correction total relative error (TRE) for the Linearized Geometric Solution and Complex Sum of four phase cycled bSSFP datasets (as in Fig. 2), with variable motion frequency and amplitude in the $\Delta\theta$ = 0° phase cycled image along the a. PE direction and b. FE direction. Sample $\Delta\theta$ = 0° motion-corrupted images are inset for specific motion frequency (10 and 50 cycles/dataset) and amplitude (3 and 28 pixels).

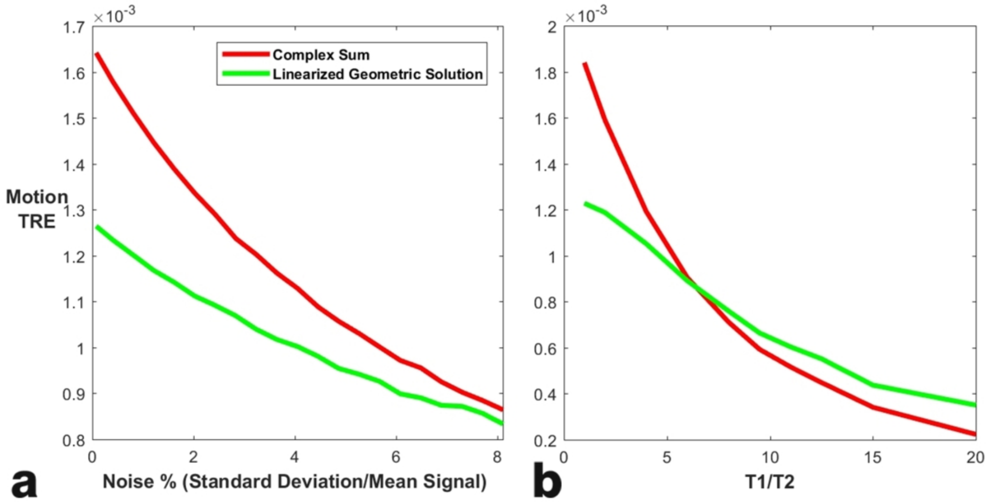

Fig.4: Motion correction Total Relative Error (TRE) for the Linearized Geometric Solution and Complex Sum of four phase cycled bSSFP datasets (as in Fig. 2) plotted for variable phase cycled image a. noise, and b. T1/T2 ratio.

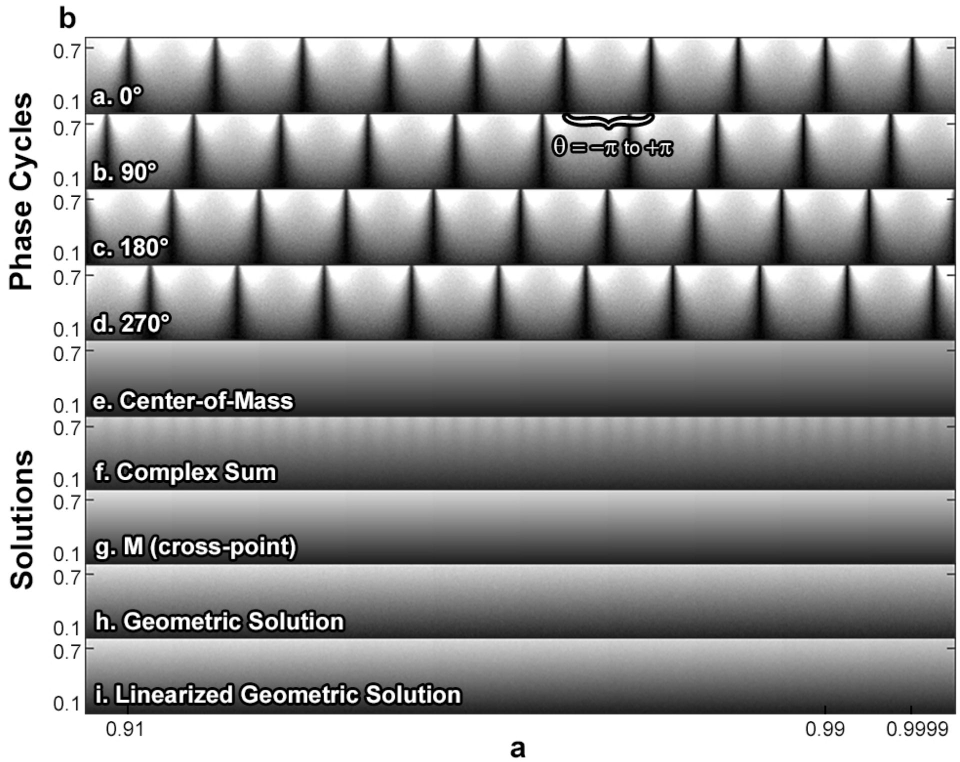

Fig.5: Simulation 2, bSSFP data with spatially varying T1, T2, and θ. a. Δθ = 0°, b. 90°, c. 180°, and d. 270° phase-cycled magnitude images. Corresponding solutions from these phase cycles are the: e. Center-of-Mass, gold standard for the f. Complex Sum, and g. Cross-point M, gold standard for the h. Geometric Solution and the i. Linearized Geometric Solution.

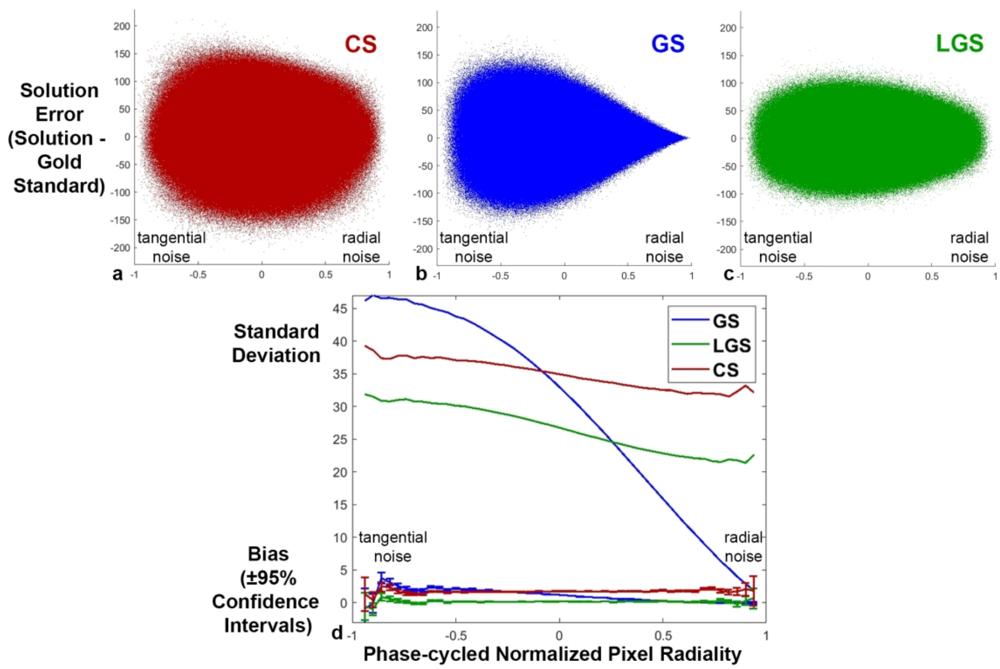

Fig.6: bSSFP a. complex sum (CS), b. geometric solution (GS), and c. linearized geometric solution (LGS) pixelwise reconstruction error cumulatively distributed as a function of noise radiality ϱ. d. CS, GS, and LGS standard deviation and bias of error from a-c plotted as a function of noise radiality ϱ. Bias includes 95% confidence interval error bars to indicate instability in regions of highly tangential or radial noise due to small sample size in corresponding bins.

177x127mm (300 x 300 DPI)

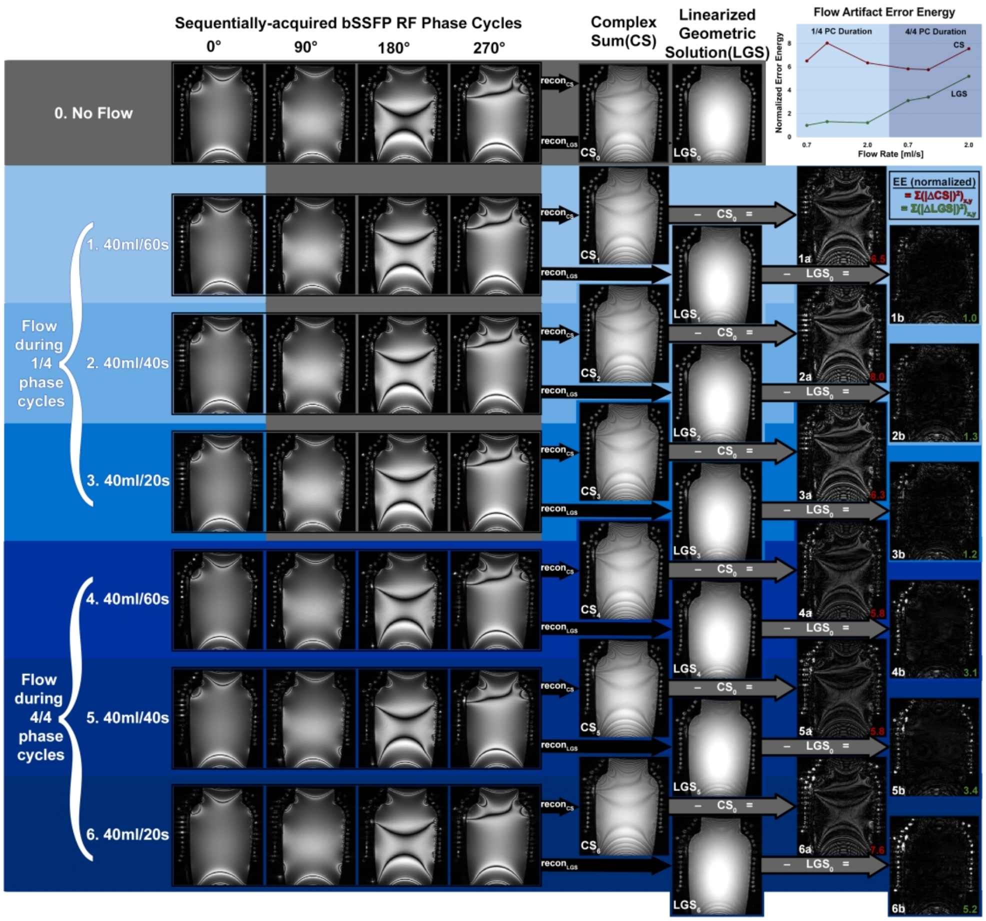

Figure.7: Four bSSFP phase cycles (PC) Δθ = 0°, 90°, 180°, and 270° are acquired of a water phantom with encircling tubes of water in 0:no-flow and six flow scenarios: 1PC (Δθ = 0°)-duration flows at 1. 40ml/60s, 2. 40ml/40s, and 3. 40ml/20s and 4PC-duration flow at 4: 40ml/60s, 5: 40ml/40s, and 6: 40ml/20s velocities. The linearized geometric solution (LGS) and complex sum (CS) are computed for each of the 7 scenarios. Flow artifact images at right (ΔCS/ΔLGS) stem from flow - non-flow differences for all 6 flow scenarios, and for each the error energy (EE) is computed, normalized, and listed. EE values are plotted vs. flow velocity at top right.

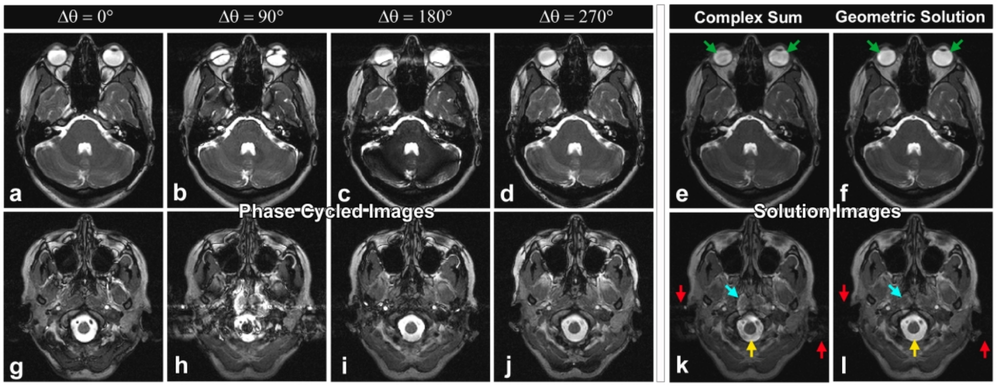

Fig. 8: Demodulation of bSSFP brain images. bSSFP axial magnitude images of the inner ear (above) and foramen magnum (below) phase cycled by $\Delta\theta$ = a) & g) 0°, b) & h) 90°, c) & i) 180°, and d) & j) 270° respectively are shown. The Complex Sum (CS) of each set of phase cycles given in e) & k) has colored arrows indicating residual banding in the CSF (yellow) and globes (green), signal modulation in the prevertebral space (blue), and motion artifact (red). Arrows of equivalent colors in the Linearized Geometric Solution (LGS) images of f) & l) demonstrate near elimination of all artifacts.

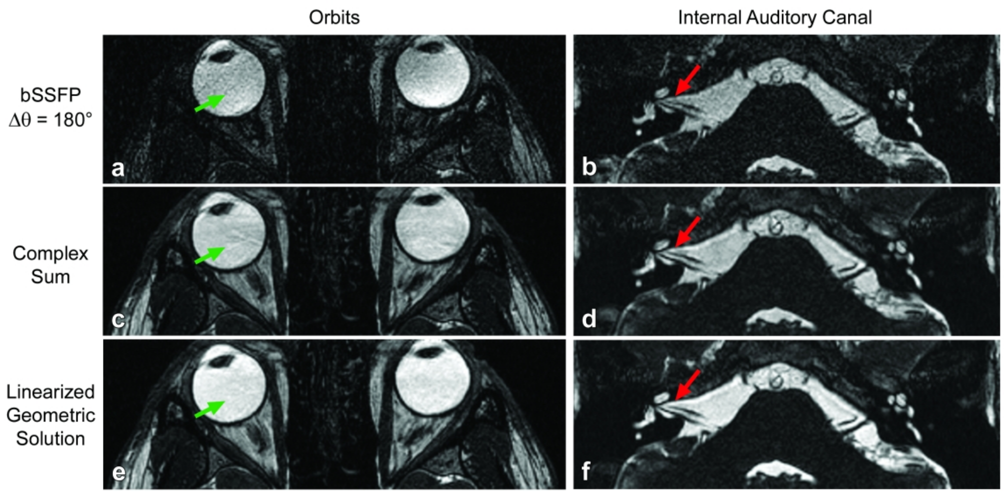

Fig. 9: Standard phase-cycled $\Delta\theta = 180°$ bSSFP axial acquisitions (a, b) are combined with three more bSSFP acquisitions ($\Delta\theta = 0°$, 90°, and 270°) to compute the complex sum (c, d) and LGS linearized geometric solution (e, f) for patient orbits (left) and the Internal Auditory Canal (IAC) (right). The LGS displays the least darkening artifact in the vitreous humor of the globes and cerebrospinal fluid in the IAC when compared with the others.

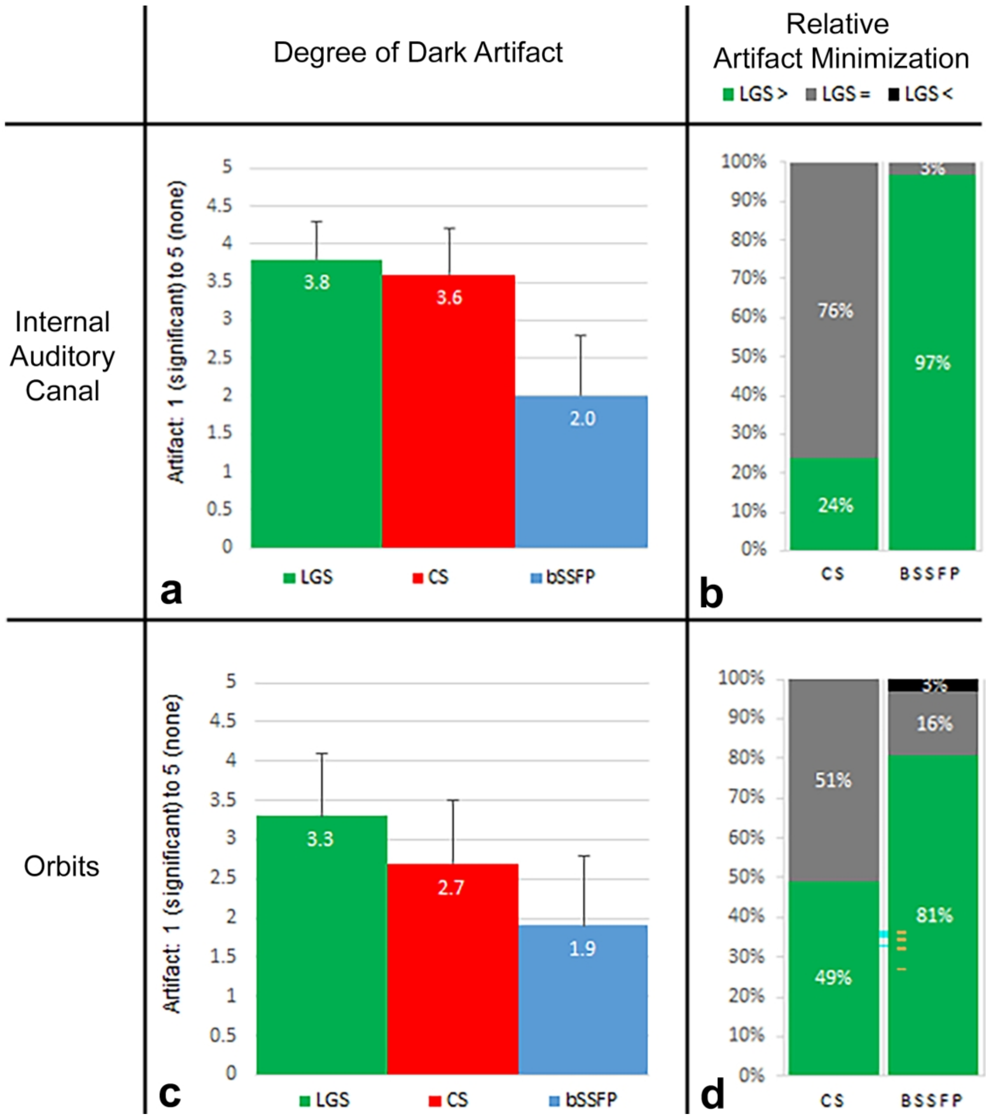

Fig. 10: Left, average degree of dark artifact is reflected for standard bSSFP, LGS, and CS reconstructions using a Likert 5-point scale from 1 = significant artifact to 5 = no artifact for a. IAC and c. orbits. Error bars indicate 1 standard deviation. Right, stacked columns show the % of reads that gauged LGS > CS or bSSFP (green), LGS = CS or bSSFP (grey), or LGS < CS or bSSFP (black) in terms of artifact minimization for b. IAC and d. orbits.

Supplementary Material for Review and Online Publication

Supporting Information Figure S1

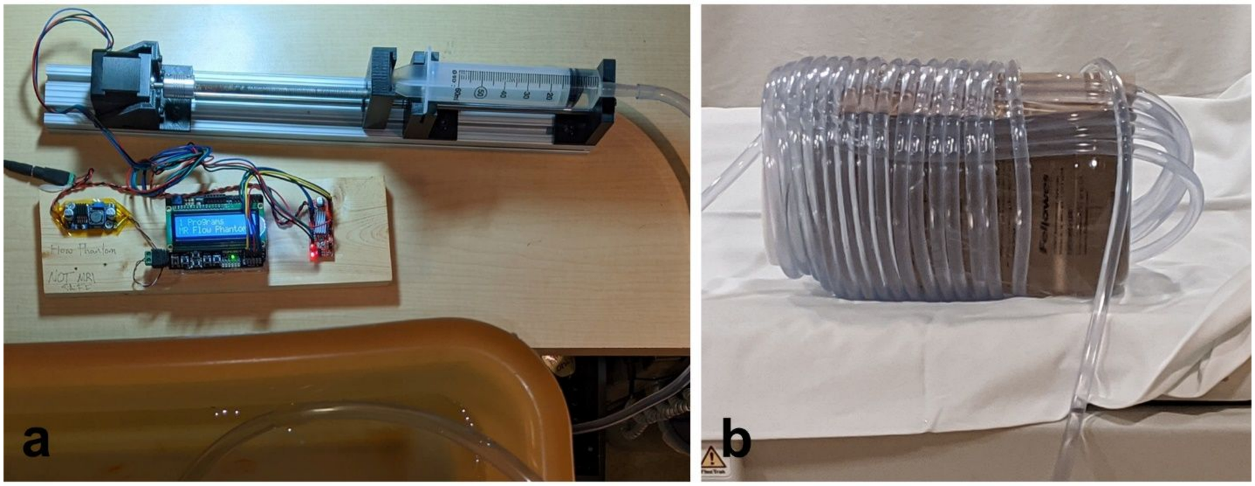

Sup. Fig. S1: a. Arduino circuit with automated controls, stepper motor, and linear actuator to oscillate syringe injection and introduce variable-speed water flow through tubes around a phantom. b. Phantom consists of flexible tubing wound around a bottle of water.